Environment Associated with Deep Moist Convection under SALLJ Conditions: A Case Study

PALOMA BORQUE*

Departamento de Ciencias de la Atmósfera y los Océanos, FCEN, University of Buenos Aires, Buenos Aires, Argentina

PAOLA SALIO AND MATILDE NICOLINI

Departamento de Ciencias de la Atmósfera y los Océanos, FCEN, and Centro de Investigaciones del Mar y la Atmósfera, CONICET, University of Buenos Aires, Buenos Aires, Argentina

YANINA GARCÍA SKABAR

National Weather Service, and Facultad de Agronomía, University of Buenos Aires, Buenos Aires, Argentina

(Manuscript received 4 September 2009, in final form 11 January 2010)

ABSTRACT

The present work focuses on the study of the environmental conditions preceding the development of a group of subtropical mesoscale convective systems over central and northern Argentina on 6–7 February 2003 during the South American Low Level Jet Experiment. This period was characterized by an extreme northerly low-level flow along the eastern Andes foothills [South American low-level jet (SALLJ)]. The entire studied episode was dominated by the presence of a very unstable air mass over northern Argentina and a frontal zone near 40°S. The SALLJ generated an important destabilization of the atmosphere due to the strong humidity and differential temperature advection. Orography provided an extra lifting motion to the configuration of the regional wind field, which was efficient in forcing the initiation of convection. Once convection developed, it moved and regenerated in regions where the convective instability was horizontally homogeneous and stronger.

1. Introduction

Environments where mesoscale convective systems (MCSs) develop have some common characteristics, including an upper-level short-wave trough, a quasi-stationary frontal zone, and a strong low-level jet (LLJ) (Maddox 1983; Laing and Fritsch 2000). Consistently, organized convection in subtropical South America develops essentially under environmental conditions characterized by synoptic-scale forcing associated with a cold front over northern Patagonia, downstream from a trough that is part of a midlevel baroclinic wave train, and thermodynamic conditions mainly characterized by a very unstable and moist air mass over southeastern South America (SESA; areas mentioned in the text are indicated in Fig. 1). Associated with these large-scale conditions, MCSs over SESA are primarily related to the presence of the South American low-level jet (SALLJ), which provides favorable dynamic and thermodynamic conditions for the development of convection over SESA (Velasco and Fristch 1987; Nicolini et al. 2002; Salio et al. 2007).

Previous papers have shown a close relationship between the SALLJ and the occurrence of precipitation over SESA (Nicolini and Saulo 2006; Salio et al. 2002; Marengo et al. 2004, among others). The presence of intense MCSs over SESA and the scarce documentation on the SALLJ were the reasons of a field experiment in South America during the warm season from November 2002 to February 2003. This study was called the South American Low-Level Jet Experiment (SALLJEX; Vera et al. 2006). During SALLJEX, a wide rain-gauge network was deployed together with enhanced aerological stations

* Current affiliation: Department of Atmospheric and Oceanic Sciences, McGill University, Montreal, Quebec, Canada.

Corresponding author address: Paloma Borque, Dept. of Atmospheric and Oceanic Sciences, McGill University, 805 Sherbrooke St. W, Montreal, QC H3A 2K6, Canada.
E-mail: paloma.borque@mail.mcgill.ca

DOI: 10.1175/2010WAF2222352.1

© 2010 American Meteorological Society

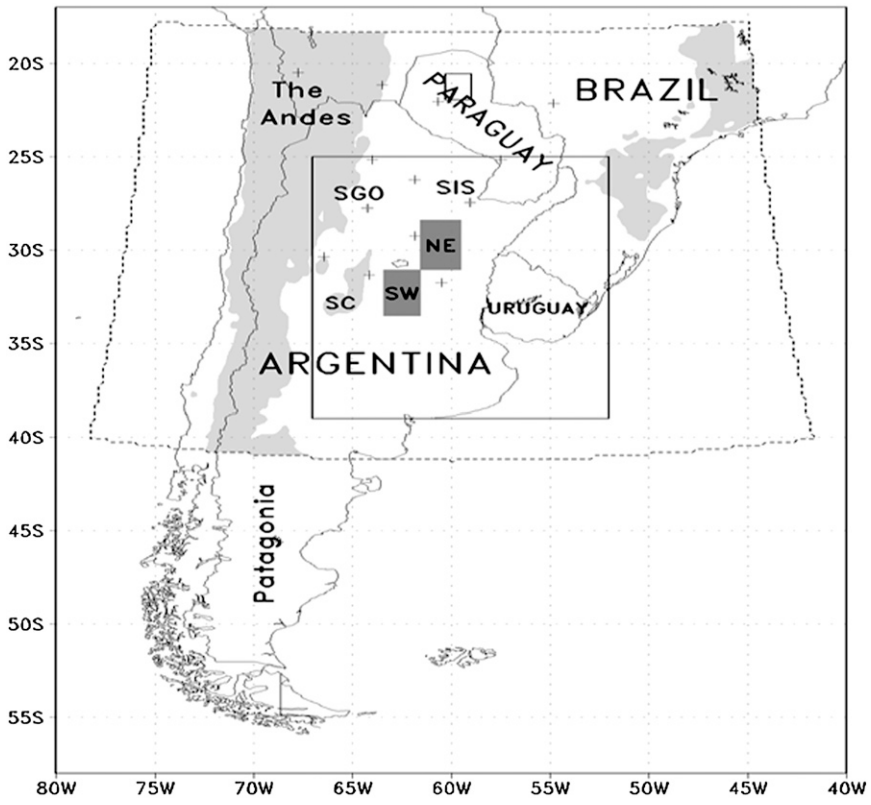

FIG. 1. Location of areas and countries mentioned in the paper: SW and NE boxes in which the temporal evolution of dynamic and thermodynamic parameters is studied (dark gray rectangles); orography higher than 800 m resolved by the model (light gray), indicating the Andes and the Córdoba Hills (SC); the model domain (dotted contour square); the region where the IR evolution is studied (solid contour square); and stations where upper-air observations were made (crosses) during SALLJEX, with the Resistencia (SIS) and Santiago del Estero (SGO) stations specially marked.

as compared with the operational network (stations where upper-air observations were made are shown in Fig. 1). This paper develops an in-depth analysis of a SALLJ situation associated with the presence of important MCSs over central Argentina occurring during the SALLJEX. The study focuses primarily on the characterization of the environmental synoptic- and mesoscale conditions that favor or inhibit the development of deep convection over central Argentina and Uruguay. Section 2 describes the criteria used to select the case study, the methodology used for the analysis, the database, and the model verification procedure. The description of the synoptic environment in which the selected case develops is presented in section 3. The convective mesoscale systems together with the associated precipitation are studied in section 4. The kinematic structure of the convection-related environment is analyzed in section 5, and the thermodynamic environment that allowed the development of the convective mesoscale systems is described in section 6. Section 7 contains a summary and conclusions.

2. Data and methodology

a. Databases

Convection generated during this event is detected using brightness temperatures from infrared channel 4 of the satellite imagery (Janowiak et al. 2001). These images have a temporal resolution of 30 min and a spatial resolution of 4 km, and the area analyzed is located between 10°–40°S and 40°–75°W. The life cycle of the systems was determined using the Forecasting Tracking of Active Cloud Clusters (ForTraCC; Vila et al. 2008) technique. Following Machado et al. (1998) and Salio et al. (2007), in order to identify areas representative of deep convection within the convective systems, areas with infrared brightness temperature values below 218 K were identified. Convective systems were defined as continuous regions of at least 150 pixels (2400 km^2) with temperatures below the selected threshold. The location and evolution of each cluster for each time were determined by means of a tracking algorithm included in

the ForTraCC technique, which assumes the continuity of the systems based on their greatest areal overlap.

Global Data Assimilation System (GDAS) operational analyses from the National Centers for Environmental Prediction, with 26 vertical levels, 1° horizontal resolution, and 6-h temporal resolution were used to analyze large-scale conditions.

Using the database of the SALLJEX experiment, a set of analyses was generated for the warm season of 2002–03, assimilating all available data. These analyses have better spatial and temporal resolutions, which allow for improving the characterization of the different case studies. Version 3.2 of the Brazilian Regional Atmospheric Modeling System (BRAMS-3.2) model was used to generate the analyses; a general description of this model can be found in Freitas et al. (2009) as well as online at http://brams.cptec.inpe.br. The data assimilation methodology included in the model, known as a 4D data assimilation scheme of the ''analysis nudging'' type, was used. This technique modifies the model fields both at the points where there are observations and over the entire grid. This procedure makes it possible to obtain 3-hourly analyses with a resolution of 80 km for almost all of South America and with a resolution of 20 km for the nested region comprising central and northern Argentina and Chile, Uruguay, Paraguay, and southern Bolivia and Brazil (Fig. 1). We used 29 vertical levels, with 18 levels in the first 12 km and the top of the model located at approximately 23 km. The assimilation process started on 13 November 2002 and was carried out continuously in order to retain in memory the previously assimilated data. The data assimilated are surface and upper-level operational network, rawinsonde, and special pilot balloon observations collected during SALLJEX. Before assimilation, coherence analyses were performed on the datasets. A more detailed description of the methodology used to obtain the analyses can be found in García Skabar and Nicolini (2009).

The characterization of MCS-related precipitation was made using ground-based observations from the SALLJEX network and Climate Prediction Center Morphed Precipitation (CMORPH) satellite estimates, with spatial resolution of 8 km and temporal resolution of 1 h [for further details on the CMORPH technique, please refer to Joyce et al. (2004) as well as online at www.cpc.ncep.noaa.gov/products/janowiak/cmorph_description.html].

b. Selection of the case study

To accomplish the goals of this work, SALLJ events that took place over SESA during the period corresponding to SALLJEX (15 November 2002–15 February 2003) were identified following the criterion considered in Salio et al. (2007). In addition, MCSs that developed in the area covered by satellite images were also identified for the same period.

The event that occurred on 6 and 7 February was selected given that it occurred during an intensive aerological observation period, implying that more data were available for assimilation into BRAMS-20. During this period, pilot balloon observations were carried out every 3 h, and at some stations radiosondes were deployed every 6 h. Furthermore, on 6 and 7 February there were two missions flown by WP-3D aircraft over the southern part of Bolivia and northwestern Paraguay. This exceptional dataset provides unique spatial and temporal resolutions for the days under study. In addition, the event occurred within an extensive SALLJ event that reached 25°S and developed deep convection over central Argentina during the afternoon of 6 February and into early 7 February.

c. Verification of the data used for the case study

For the event under study, GDAS and BRAMS-20 analyses were validated against the data from the WP-3D missions (see online at http://www.nssl.noaa.gov/projects/pacs/salljex/p3/), which were not included in the assimilation process and therefore the following comparison is completely independent.

Between 1730 and 1838 UTC 6 February, WP-3D aircraft recorded seven vertical profiles of different atmospheric variables between 20.57°–21.96°S and 58.98°–60.30°W. The profiles of the temperature, dewpoint, and meridional and zonal wind components were averaged in time and in the vertical (each 100 m) to generate one smoothed profile representative of the area. The smoothed profiles were then compared with 1800 UTC spatially averaged profiles from GDAS and BRAMS-20 analyses. The spatial average was calculated so that the location of the aircraft fell within the rectangle of the smallest possible area given the resolution of each analysis. Thus, the performance of each model could be evaluated by taking into account its resolution against the data recorded by the aircraft. Both sets of analyses adequately reproduced the behavior of the different variables in the vertical (Fig. 2b); however, GDAS at 1800 UTC represents the thermodynamic structure of the atmosphere better in comparison with BRAMS-20 at near-surface levels (Fig. 2b). In addition, BRAMS-20 analyses were compared with the profile centered at 19.7°S, 59.7°W, obtained from another flight of the WP-3D made on the same day at 1500 UTC. This comparison showed similar performance as that for 1800 UTC, but with a better representation of the thermal structure of the atmosphere (Fig. 2). The observations obtained by the aircraft are close to the northern limit of the BRAMS-20 grid and no sounding is available to assimilate over that region, suggesting that no improvements

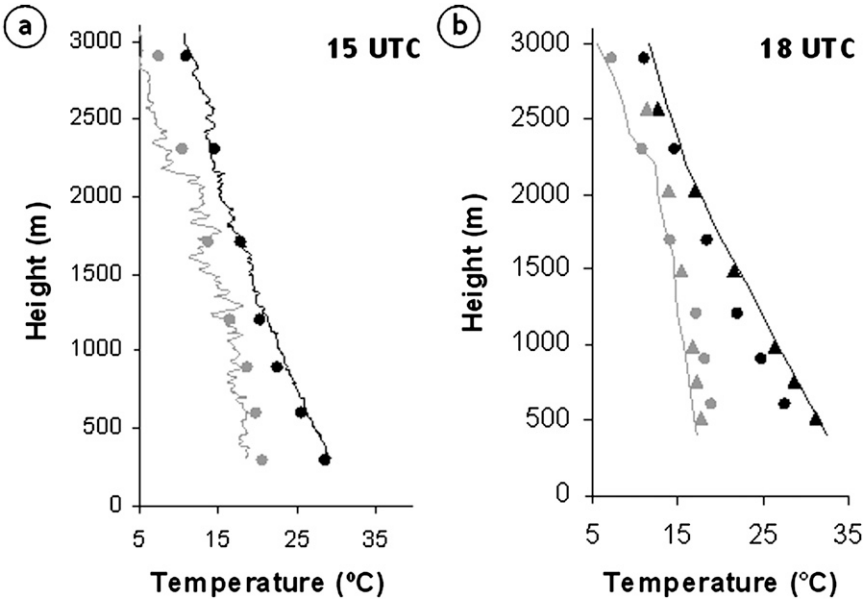

FIG. 2. Vertical profile of temperature (°C, black) and dewpoint temperature (°C, gray), for data from WP-3D aircraft (solid), BRAMS-20 (circle), and GDAS (triangle) at (a) 1500 and (b) 1800 UTC 6 Feb. The profile was calculated over the area between 21.96°S, 58.98°W and 20.57°S, 60.30°W.

can be expected in the BRAMS-20 performance as see in Fig. 2a.

To evaluate the behavior of GDAS and BRAMS-20 data in the central area of the grid (central Argentina), the vertical wind and/or thermodynamic profiles resulting from the analysis were compared with radiosonde observations launched at 0600 and 1800 UTC 6 and 7 February at the Resistencia and Santiago del Estero stations.

BRAMS-20 positioned well the height of the maximum of the meridional wind component and the maximum wind speed at 0600 UTC 6 February in Santiago del Estero station (Fig. 3); however, it underestimates its intensity. On the other hand, the GDAS profile, consistent with the nondata assimilation, shows a greater departure from the sounding as it locates the maximum wind intensity near the surface. This result underscores the importance of data assimilation over the area, which is consistent with García Skabar and Nicolini's (2009) results for SALLJEX stations located in areas in proximity to topography.

The BRAMS-20 representations of temperature and dewpoint, from the surface up to 4000 m, are very similar to the observations, and they are much better than

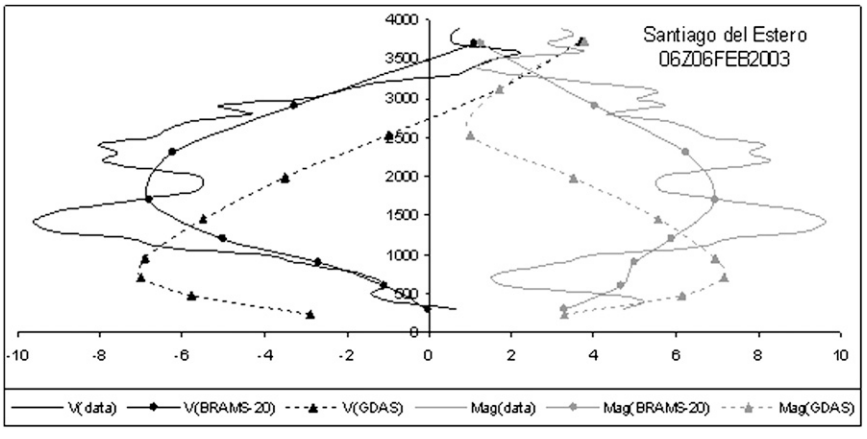

FIG. 3. Vertical profile of the meridional wind speed (m s^{-1}, black) and total wind speed (m s^{-1}, gray) for data measured at the Santiago del Estero station (solid) and for the closest grid point in BRAMS-20 (solid with circles) and GDAS (dashed with triangles) at 0600 UTC 6 Feb.

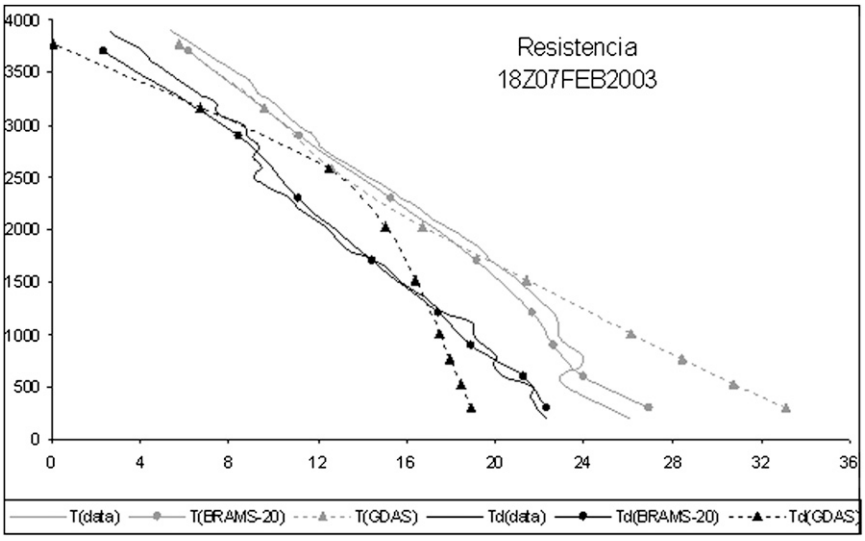

FIG. 4. Vertical profile of temperature (°C, gray) and dewpoint temperature (°C, black) for SIS data (solid) and for the closest grid point in BRAMS-20 (solid with circles) and GDAS (dashed with triangles) at 1800 UTC 7 Feb.

the GDAS analyses, particularly at 1800 UTC 7 February in Resistencia (Fig. 4). A similar pattern of behavior is observed at the Santiago del Estero station (figure not shown). Therefore, BRAMS-20 presents a better representation of what happened at both stations than GDAS, giving very good results in the entire layer from the surface up to 4000 m, especially for the Resistencia station. Such a high space–time resolution dataset can improve our knowledge of the mechanisms that influence the development of convection.

3. Description of the synoptic environment

To understand the evolution of the different variables on the synoptic-scale GDAS, data fields at 0000 UTC 6 and 7 February 2003 are shown in Figs. 5–8. At 1000 hPa (Fig. 5) over northwestern Argentina near 26 °S, the northwestern Argentinian low (NAL; Seluchi et al. 2003) is present on both days, reaching its maximum extension and intensity on 7 February. This favors a strong northerly low-level flow (Fig. 6) from Bolivia up to 30°S that, as

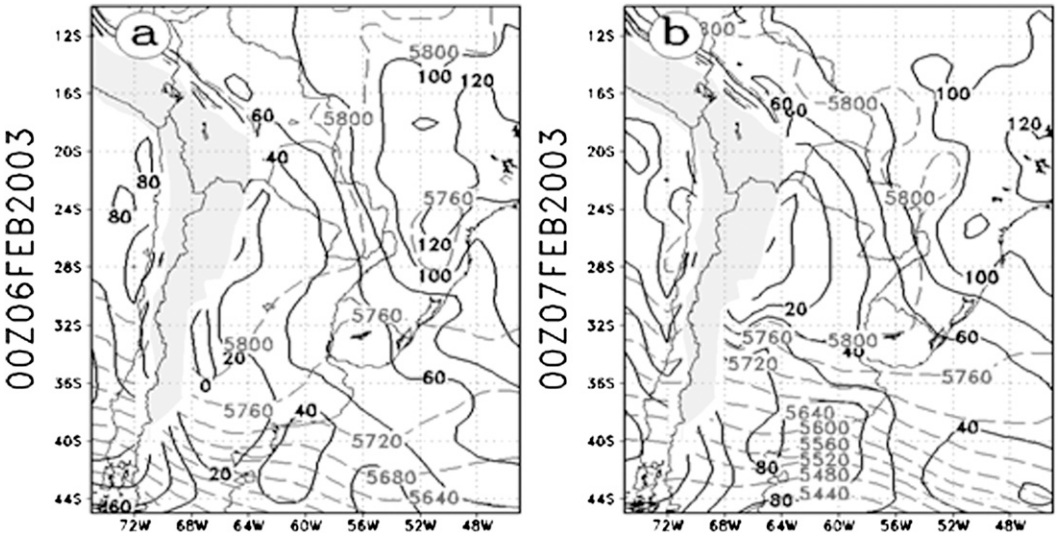

FIG. 5. The 1000-hPa geopotential height (gpm, solid) and 500–1000-hPa thickness (every 60 gpm, dashed) at 0000 UTC (a) 6 Feb and (b) 7 Feb. Values where topography is above 1500 m have been masked.

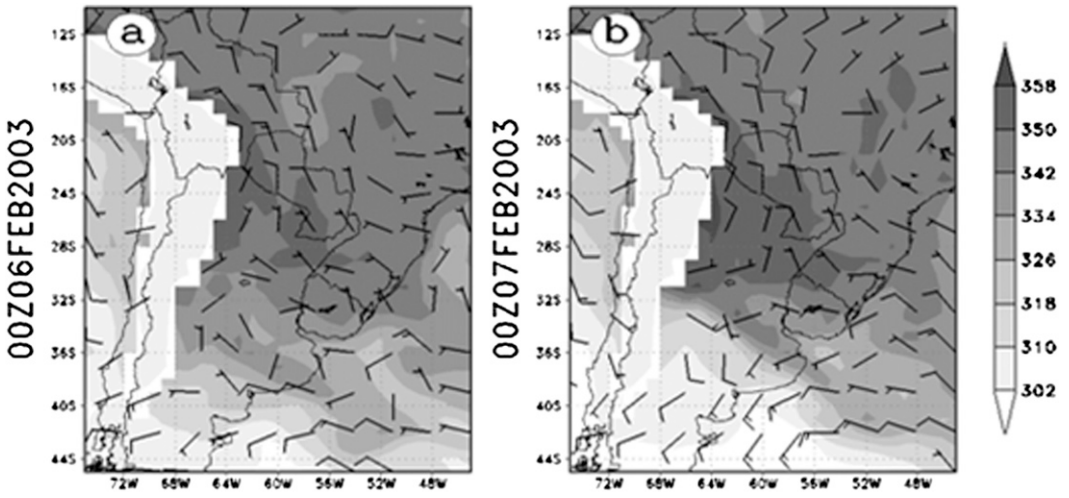

FIG. 6. The 850-hPa θ_e (every 4 K, shaded) and wind speed (m s^{-1}, barbs) at 0000 UTC (a) 6 Feb and (b) 7 Feb. Values where topography is above 1500 m have been masked.

shown below, displays SALLJ characteristics. During the studied period, the evolution of a cyclonic vorticity perturbation (Fig. 7) associated with a frontal zone can be observed at 500 hPa. This perturbation is also detectable at lower levels in both the thickness and the equivalent potential temperature θ_e fields (Fig. 6). The strong θ_e gradient is located over northern Patagonia and indicates the position of a baroclinic area that moves up to 30°S on 7 February.

At higher levels, there is a 500-hPa long-wave trough (Fig. 7) located upstream of Patagonia with the corresponding advection of cyclonic vorticity over central Argentina that favors large-scale upward motion over the region. At 200 hPa (Fig. 8), the area where the convective system develops is located at the anticyclonic entrance of the upper-level jet; the position and evolution of the MCSs over central Argentina will be analyzed in section 4. Therefore, large-scale upward motion was favored from both upper-level divergence associated with the entrance of the upper-level jet and differential cyclonic-vorticity advection over the region where MCSs develop and evolve.

The structure of the synoptic field observed in this case study is very similar to that found in the composites calculated by Salio et al. (2002), Marengo et al. (2004), and Salio et al. (2007). Among the similarities are the southward extension of the low pressure system associated with the surface NAL and the presence of a strong northerly flow over the northern region of Argentina, Paraguay, and southern Brazil at 850 hPa. Liebmann et al. (1999) showed similar mechanisms for uplift as those described in this paper; among them is the mechanical element provided by the frontal zone and the upper-level vorticity advection over the region. Another necessary ingredient present in both works is the advection of higher values of moisture from the Amazon Basin. Garreaud and Wallace (1998) and Garreaud (2000) showed a strong connection between a frontal surface and the development of deep convection, especially for spring and summer cases. The

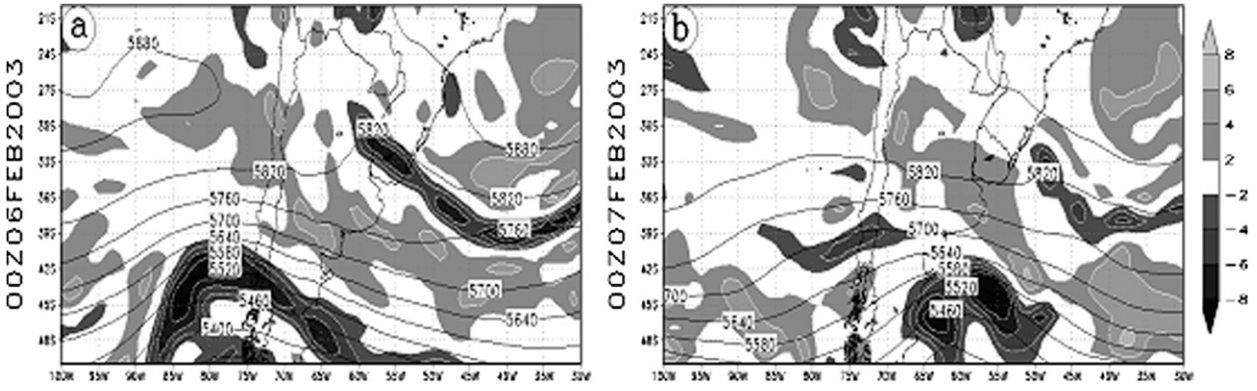

FIG. 7. Relative vorticity ($\times 10^{-5}$ s^{-1}, shaded) and geopotential height (gpm, contour) at 500 hPa at 0000 UTC (a) 6 Feb and (b) 7 Feb.

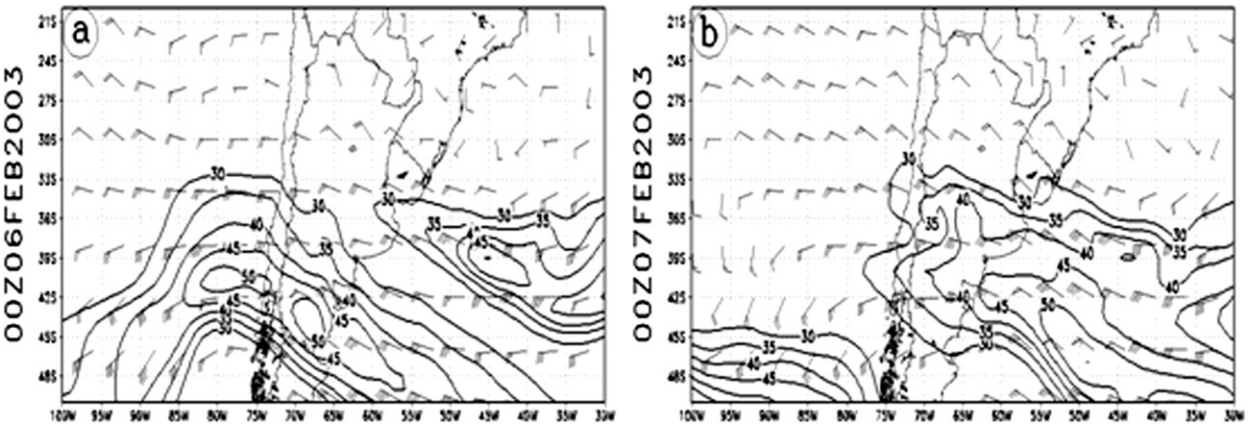

FIG. 8. Wind speed (m s^{-1}, barbs) and wind speed greater than 30 m s^{-1} (contours) at 200 hPa at 0000 UTC (a) 6 Feb and (b) 7 Feb.

present case study shows more extreme values of potential temperature θ and low-level wind speed both at low and high latitudes than the composites.

4. Evolution of convection and associated precipitation

One of the purposes of this paper is to study the evolution of different MCSs that developed during nocturnal and morning hours. Figure 9 shows the temporal evolution of the infrared brightness temperature over SESA, and Fig. 10 shows the size evolution of all systems detected over the area. In spite of the persistence of SALLJ conditions, 6 February is characterized by the absence of subtropical convection in the area between the Andes and 55°W up to 1900 UTC possibly related to the diurnal heating cycle but also to the fact that in the early hours of 6 February the low-level wind presents a westerly

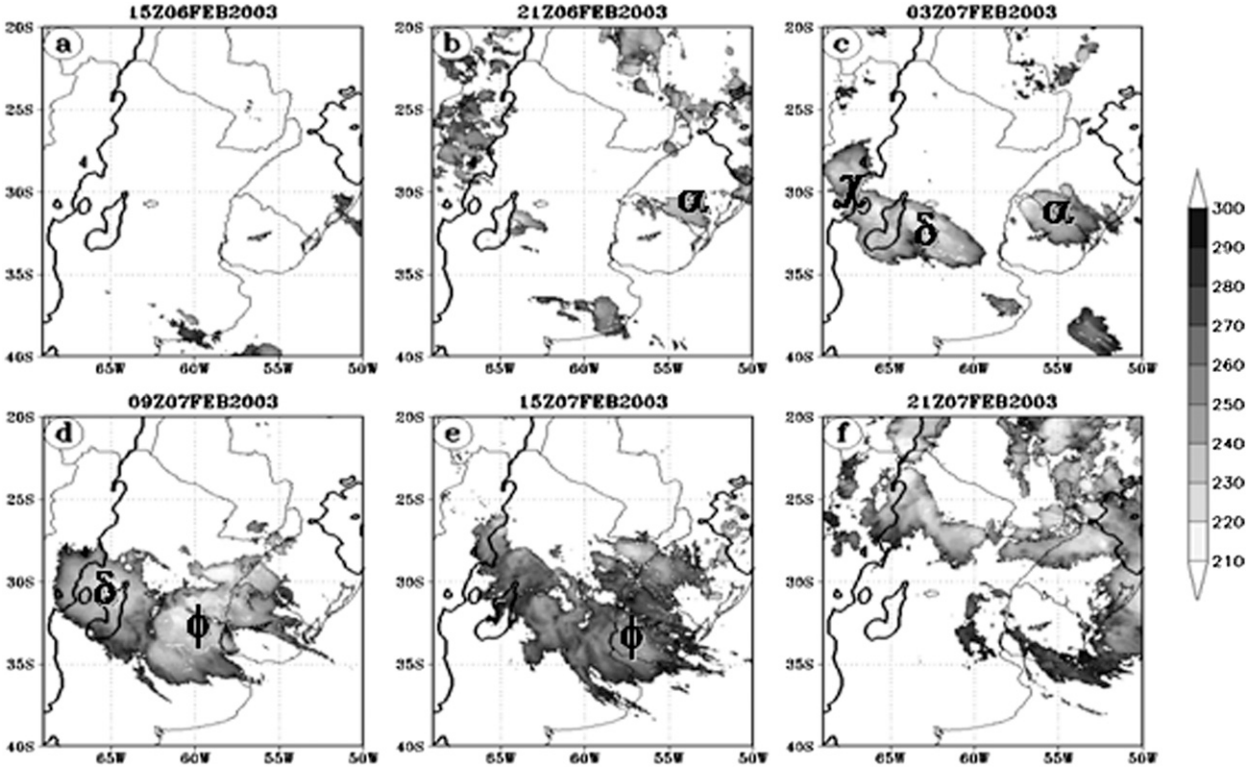

FIG. 9. Brightness temperature (°C) every 6 h from (a) 1500 UTC 6 Feb to (f) 2100 UTC 7 Feb, with the name of the systems identified by ForTraCC indicated in Fig. 10 and 800-m orography (black contour).

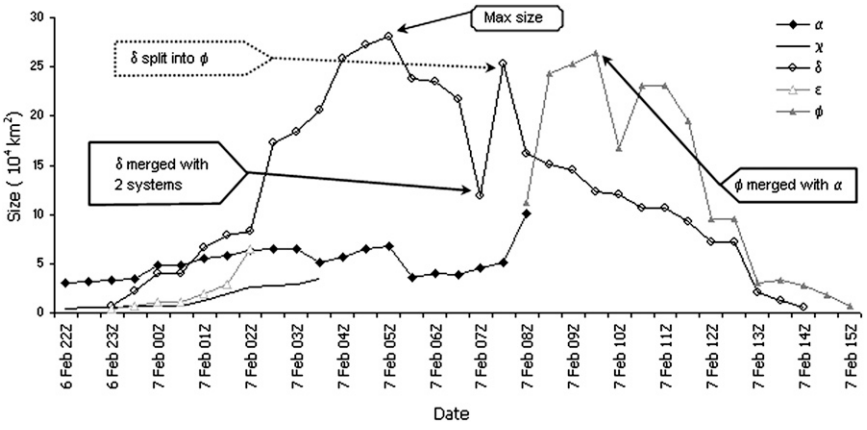

FIG. 10. Temporal (every 1 h) evolution of convective cell sizes occurring between 2200 UTC 6 Feb and 1500 UTC 7 Feb, with the main moments of the MCSs denoted.

component (Fig. 6a), implying that less humidity was being advected to the region under study. Also, as will be seen in the following sections, during the afternoon of 6 February the SALLJ orientation is more meridional, producing an increase in the mixing ratio values at 1800 UTC 6 February, the moment when convection is triggered.

At 1900 UTC 6 February, the first convective cell—called α—was generated over northern Uruguay. During its life cycle, this cell presented the coldest top temperatures along its western side, indicative of a predominant development of new intensive cells over its western flank (Fig. 9c). The system called χ started its life cycle at 28.7°S, 67°W at 2200 UTC (Fig. 10) and remained quasi-stationary over the mountains (Fig. 9c). New MCSs arose over the center of Argentina at 2300 UTC (Fig. 10), ε over the eastern side of the Córdoba Hills and δ to the west of ε. At 0500 UTC 7 February, after merging with ε and χ, the 218-K contour representative of the δ MCS reached an extent of 280 432 km^2, which is the greatest of all the MCSs in the analyzed period (Fig. 10). From that moment, it abruptly decreased in size until it merged with other convective cells present over the center of the country, giving rise to a secondary maximum of 253 000 km^2 at 0730 UTC (Fig. 10). At this time, δ started its final reduction in size mainly due to a split that produced the MCS indicated as ϕ (Figs. 9d and 10). Later, ϕ merged with α, resulting in a clear increase in the area covered by ϕ (Fig. 10). The dissipations of δ and ϕ occurred at 1230 UTC 7 February when their sizes became smaller than the 50 000 km^2 threshold (Fig. 10). It is important to point out that over the region where MCSs develop the minimum infrared temperature is reached at 1800 UTC (1500 local time).

The comparison of the location of the MCSs with the location of the maximum convection frequency found by Salio et al. (2007) reveals that in the present study the MCSs were located toward the south and did not present their classical propagation to the northeast during their life cycles. As for the starting time, the time at which MCS δ developed is included in the interval of the highest MCS starting frequency found by Velasco and Fristch (1987), Laing and Fritsch (2000), and Salio et al. (2007). The same is observed in connection with the size at the time of maximum expansion, since this size is close to the size that corresponds to the greatest frequency, according to these authors. It is worth mentioning that although Salio et al. (2007) analyzed the occurrence of MCSs related to the presence of SALLJ during the period 1 September 2000–31 May 2003, the largest MCS studied in this paper was not included in their composites, as it underwent numerous mergers and splits with other systems during its life cycle.

To evaluate the impacts of MCSs on the precipitation field, Fig. 11 presents the 24-h accumulated rainfall field at 1200 UTC 7 February. The data shown belong to the SALLJEX network, BRAMS-20 24-h forecasts, and CMORPH satellite estimates. On 7 February there is an important lack of information over the central area of Argentina due to the scarce coverage of the rain-gauge network in this region, although some extreme values over the eastern part of the country are found. Ruiz (2010) analyzed CMORPH's performance during the SALLJEX period and showed a good estimation of precipitation but with a slight underestimation of values greater than 50 mm h^{-1}. Given that CMORPH precipitation estimates reproduce accurately the areas where rainfall was observed as well as the maximum values, they were included in the analysis for a better comparison with BRAMS-20 in the regions lacking precipitation data.

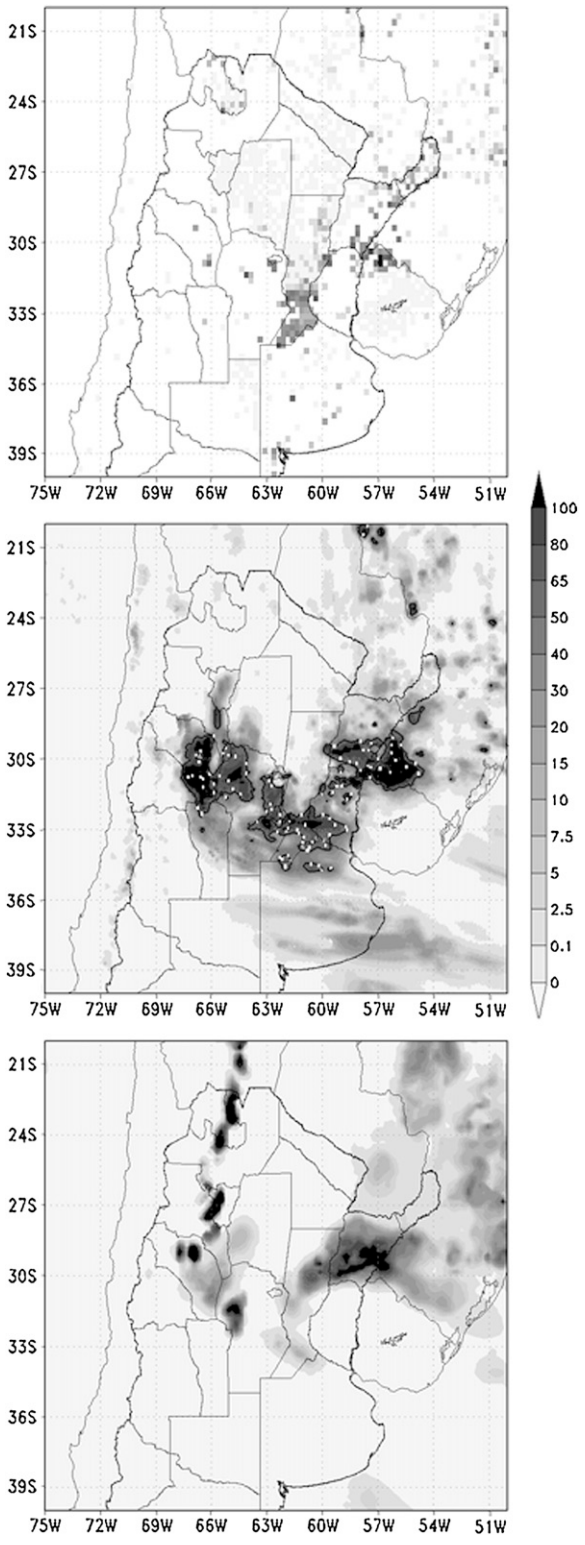

FIG. 11. Rainfall (mm h^{-1}) measured by (upper panel) the SALLJEX network and (middle) the BRAMS-20 24-h forecast and (bottom panel) estimated with CMORPH (right column), accumulated at 1200 UTC 7 Feb.

Compared with the CMORPH dataset, BRAMS-20 during this episode systematically overestimates the precipitation observed on the eastern slope of the Andes north of 30°S (Fig. 11). Even though it does not seem to reflect perfectly well what happens near the orography, it is the only source of information available. Rainfall over west-central Argentina on 7 February is underestimated by BRAMS-20; however, it is difficult to evaluate the location of the rainfall maxima given by the model in the central area of Argentina due to the scarce coverage of the rain-gauge network in this region.

Comparison between Figs. 9 and 11 shows that the underestimation is due to the fact that BRAMS-20 seems to not be able to resolve the rainfall resulting from system δ in central Argentina. An examination of the cloud coverage patterns (not shown) revealed the presence of clouds in the region where convective system δ developed, and as will be seen in the following sections, significant unstable conditions were captured well by the model even if it failed to produce precipitation as observed. The satisfactory evaluation of thermodynamic profiles gave us confidence in pursuing the instability analysis further and motivated the analysis produced in section 6 where different regions where selected: one where the MCS developed, probably characterized by more unstable conditions than were reproduced by the analyses, and another where the system propagated and new cells occurred, which was well simulated by the model.

5. Kinematic structure of the convection-related environment

Figure 12 presents the vertical profiles of the meridional wind speed and θ at 25°S obtained from BRAMS-20. The latitude selected for these profiles is located northward from the location of the MCSs before and after they developed. It is worth mentioning that the low-level jet profile is present to the north of Argentina during the entire period under study, as well as during the previous days (figure not shown). An important feature of the thermodynamic structure of the atmosphere is that the height of the boundary layer is closely related to the level at which the maximum wind speed occurs. Both levels evolve consistently in the vertical during the daily cycle. Clear examples occur at 1800 UTC 6 and 7 February, when the boundary layer deepens above 1500 m and is capped by wind speeds greater than 12 m s^{-1} (Fig. 12). Although the wind speed decreases in the evening, the northerly flow persists, indicating the presence of a larger-scale pressure gradient over the area favoring northerly winds. In the period comprising the genesis and maximum development stages of the MCSs, the maximum wind speed increases while it moves downward. At 1800 UTC 6 February it is

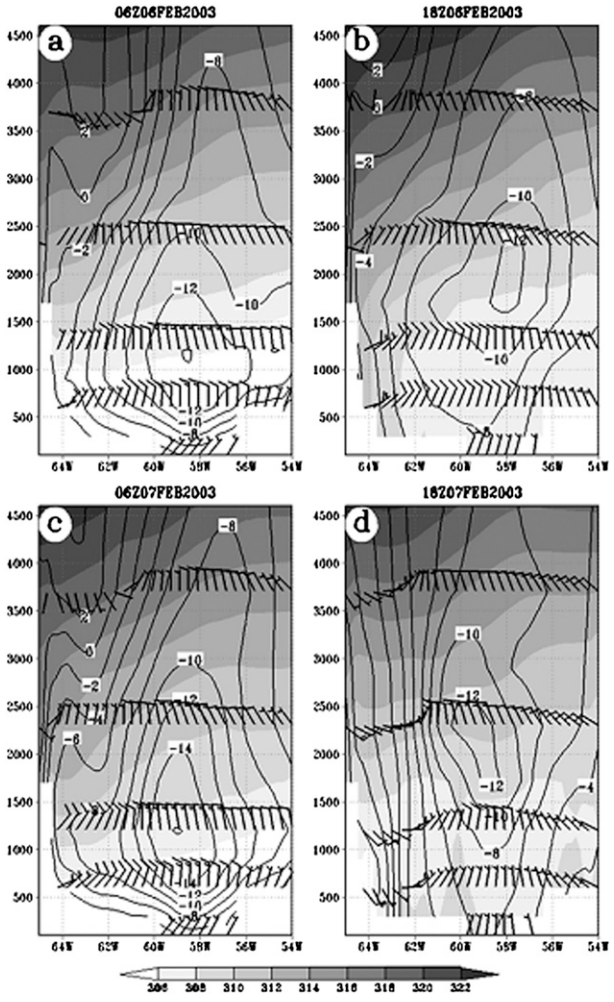

FIG. 12. Vertical section of θ (K, shaded), wind speed (short barb represents 5 m s^{-1}; long barb represents 10 m s^{-1}), and meridional wind component (m s^{-1}, black contour) at 25°S every 12 h from (a) 0600 UTC 6 Feb to (d) 1800 UTC 7 Feb. All panels stretch longitudinally from 66° to 54°W.

located at approximately 2000-m height, with a speed exceeding 12 m s^{-1}, while 12 h later, the maximum wind speed is found at 1200 m and is stronger than 16 m s^{-1} near 59°W (Fig. 12). An important fact is the slowing down of the SALLJ to the south of 25°S, which indicates strong convergence at low levels in the area downstream of the maximum wind intensity (figure not shown).

6. Thermodynamic structure in the MCS region

Positive advection of specific humidity q over the eastern slope of the Córdoba Hills was observed during the 24 h prior to the development of the MCSs (Figs. 13b–d). The change in wind direction recorded during that day allows one to assume that the moisture increase is also

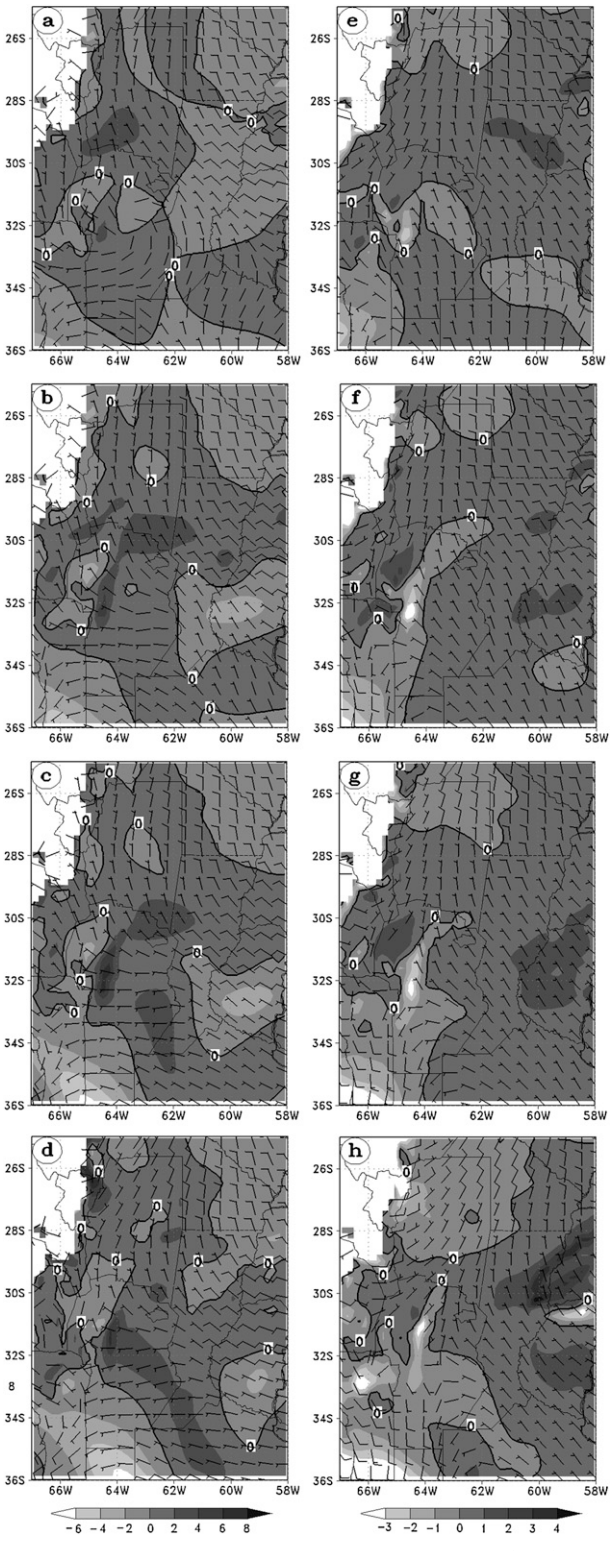

FIG. 13. Horizontal advection of (a)–(d) q (g kg^{-1} h^{-1}) and (e)–(h) temperature (°C h^{-1}) at 2300 m along with wind speed (m s^{-1}, barbs) at the same level every 3 h from (up) 0900 to (bottom) 1800 UTC 6 Feb.

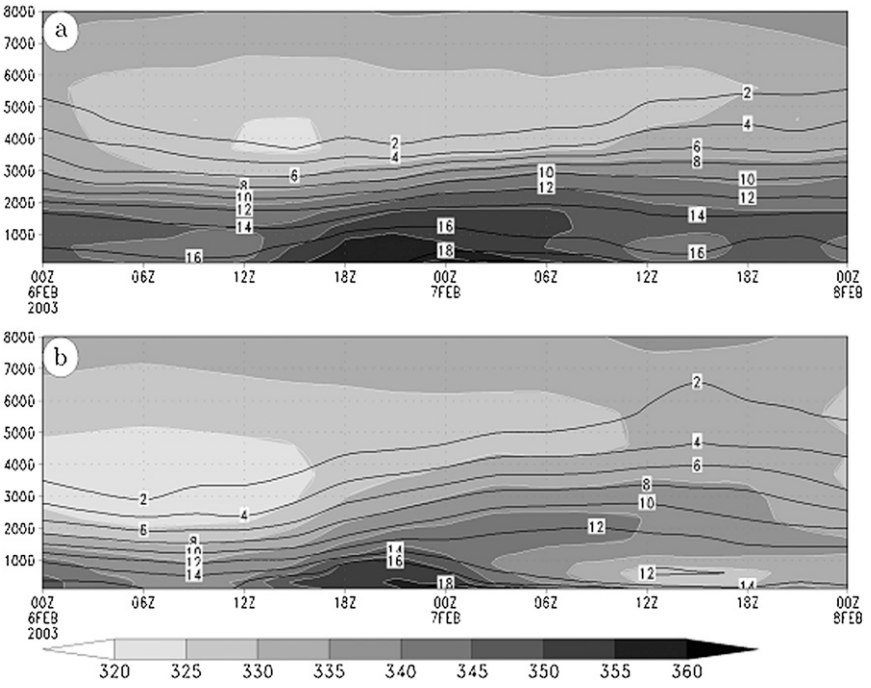

FIG. 14. Evolution of θ_e (every 5 K, shading) and q (g kg^{-1}, contours) from 6 to 7 Feb as a function of height (m), for the (a) NE and (b) SW areas.

related to the flow convergence caused by the blocking effect of the orography. Consistent with the presence of the baroclinic zone previously described, values of specific humidity advection at 2300 m show the presence of a well-defined NW–SE transition area; however, this feature cannot be seen in the temperature advection field at the same level. An important point is that while the generated convection received a great input of moisture, it was inhibited by the temperature advection field, since the area at 2300 m was dominated by cold advection (Figs. 13e–h). Differential thermal advection, however, had a major role in the destabilization of the region as horizontal thermal advection below 2300 m reached positive values while decreasing with height (figure not shown).

Two geographic domains are defined to characterize the mesoscale environment in the area where the MCSs developed and in the area toward which they later moved. As the genesis region of the MCSs is located on the western slope of the Córdoba Hills, the average for the genesis region is displaced to the east so as to avoid the slope, thus achieving more reliable values of the variables at lower levels. In both the selected and the genesis area, most processes and values recorded for the different variables are comparable. The exception is in convergence, which is larger at the genesis area because of the blocking effects of orography. Bearing this in mind, the region selected to represent the genesis area is the one limited by 33.5°–31°S and 63.5°–61.5°W (SW zone). The representative region for the characteristics of the area toward which MCSs move once they have entered the mature stage is northeastward of the previous one and located between 31°–28.5°S and 61.5°–59.5°W (NE zone). The mentioned regions are denoted in Fig. 1.

Figure 14 shows the temporal evolution of θ_e and the specific humidity averaged in the NE and SW boxes. On 6 February there is a decrease of θ_e at the midlevels, as a consequence of the drying process that took place in the area from 0900 UTC (Fig. 14). The drying process was much more marked in the SW area (Fig. 14b). Such midlevel drying can be related to descending motions associated with the ridge present during that day in the study area (Fig. 7). A marked rise in θ_e is observed at low levels in both areas from 1500 UTC (Fig. 14). The rise is mainly related to increased θ associated both with radiative heating and SALLJ-related warm advection (located below 2300 m). Above 1500 m, the increase in specific humidity starts gaining importance, as a result of the strong SALLJ-related humidity advection. Although the depth of the unstable layer did not increase at 2100 UTC, θ_e reached an extreme value of 355 K at the surface and of 348 K at 1200 m (Fig. 14a). These values show the characteristics of a warm and humid air mass that undergoes major changes in 24 h, with an increase of more than 10° due to the clear influence of θ and q advection at lower levels. Concerning the NE region, there is an important increase in convective instability at 1200 UTC 6 February,

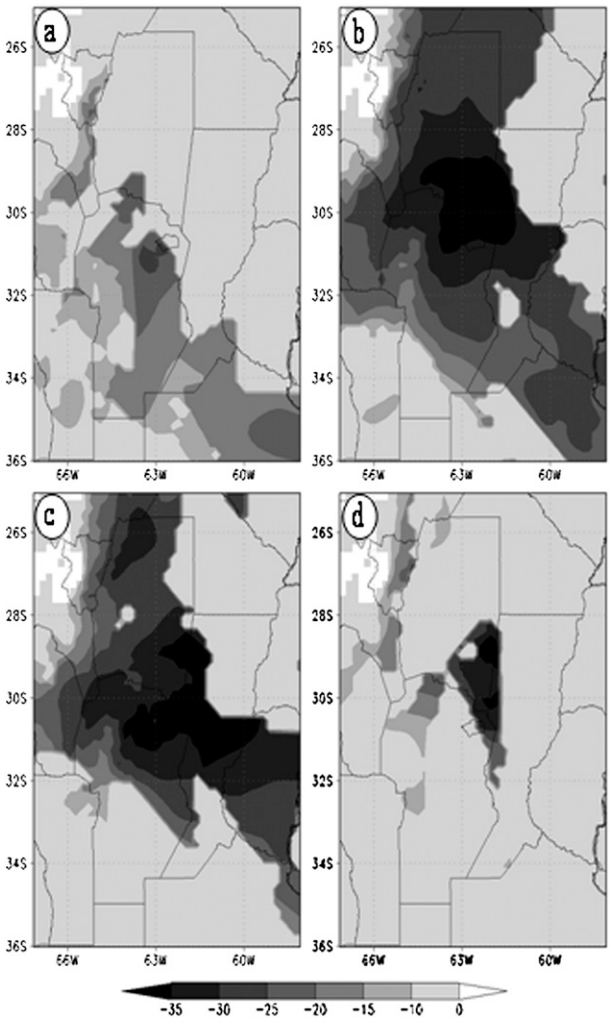

FIG. 15. Vertical variation of θ_e (K) between the base and the top of the unstable layer every 6 h from (a) 1200 UTC 6 Feb to (d) 0600 UTC 7 Feb.

which is maximized between 0000 and 0300 UTC of the following day and which is stronger with respect to the area previously described (Fig. 14a). Contrary to what happens in the SW zone, the temporal evolution of the thermodynamic characteristics of the area is not as marked (Figs. 14a and 14b).

Convective stability field

The well-known concept of convective instability allows us to explore the potential occurrence of conditions favorable for increased instability if some sort of forced ascent of a layer is present and requires a decrease in the equivalent potential temperature through that layer. Examination of Fig. 15, which displays the spatial distribution of the thickness where the vertical variation of θ_e is negative with height ($\Delta\theta_e < 0$), shows a decrease in θ_e with altitude, which became more marked during the morning of 6 February.

Major $\Delta\theta_e < 0$ values are concentrated in the northern part of the area where the first studied MCSs developed (Figs. 15a–c). The zone of extreme $\Delta\theta_e < 0$ presents differences exceeding −35° between the base and the top of the unstable layer (Figs. 15b and 15c). This zone comprises a thickness of nearly 3500 m with the base of the unstable layer near the surface (figure not shown). Furthermore, the thickness of the layer with the largest variation in θ_e values, centered over 30°S, 63°W, is similar to that of the surrounding region; therefore, the convective instability in the area where the MCSs developed is considerably stronger than in the surroundings.

The instability characteristics of the air mass were studied by means of the mean, minimum, and maximum convective available potential energy CAPE and convective inhibition (CIN) values reached in the regions previously studied and corresponding to the available potential energy of the surface parcel. From 0000 UTC 6 February through the next 9 h, CIN starts increasing while CAPE decreases in the SW zone (Fig. 16a). CAPE reaches its minimum value (zero) and CIN its maximum (500 J kg^{-1}). The latter then decreases and remains very close to zero from 1500 UTC 6 February until the same time on the following day. It is worth highlighting that the sudden increase in CAPE between 1200 and 1500 UTC 6 February was more than 3600 J kg^{-1} in 3 h, reaching values above 4000 J kg^{-1}; the average value in the entire region, however, remained far below 1500 J kg^{-1} (Fig. 16a). The radiosonde observation at the Chamical station (30.22°S, 66.17°W) for this day at 1800 UTC reveals a CAPE value above 4000 J kg^{-1}, which is consistent with the values obtained from BRAMS-20. The maximum value for the entire period occurred between 0000 and 0300 UTC 7 February and was greater than 4500 J kg^{-1}, but its difference from the mean value (1000 J kg^{-1}) was even greater. This difference in CAPE values is important at 0600 and 0900 UTC 7 February, when the mean CAPE was very close to zero, while the maximum was approximately 2500 J kg^{-1}. This shows that the instability is very localized in the origin region with a large spatial variability between 1500 UTC 6 February and 1200 UTC of the following day (Fig. 16a).

In the NE region, the evolution of CIN is very similar to that in the SW zone. The major difference between the two regions is the fact that mean and maximum CAPE values are similar over the NE region during the entire period. Between 0000 and 0300 UTC 7 February the behavior of the instability is remarkable, given that the difference between the maximum and minimum CAPE values is smaller than 1500 J kg^{-1} (Fig. 16b). This

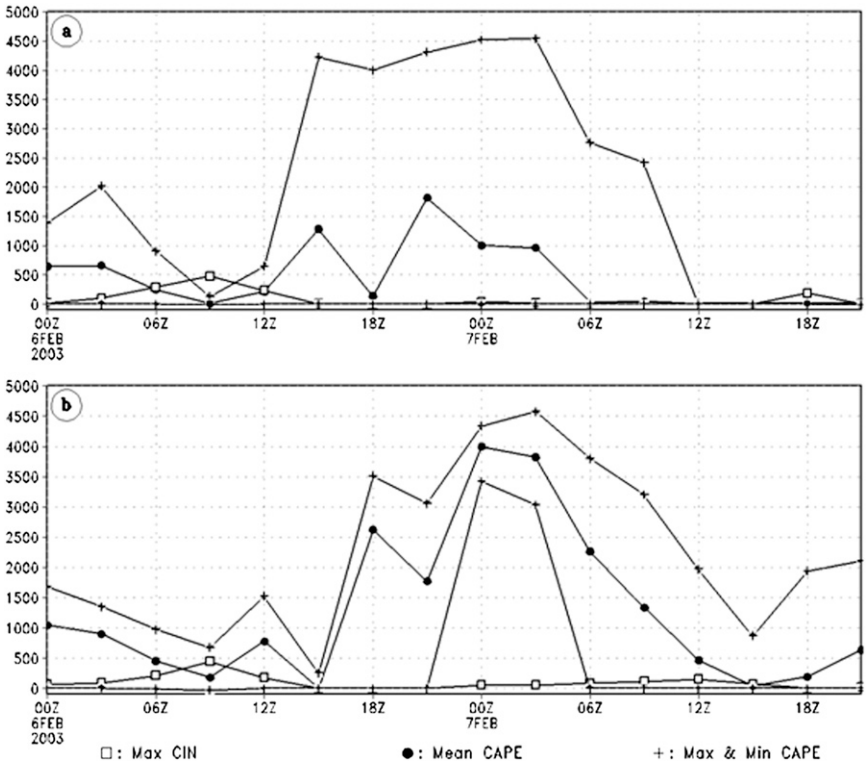

FIG. 16. Simulated mean CAPE (circles), maximum CIN (squares), and maximum and minimum CAPE (crosses) reached at each time anywhere in the (a) SW and (b) NE regions. Units are J kg^{-1}.

shows that in terms of instability this area is more homogeneous than the SW zone, which makes development possible in the entire area under study and not only in isolated areas, as occurred in the genesis zone.

7. Conclusions

The days analyzed in the present case study are during the summer season of 2002–03 and present an anomalously long period of 11 consecutive days (31 January–10 February 2003) under SALLJ conditions. This period marks the second longest SALLJ conditions during SALLJEX, being surpassed only by the successive 15 days of SALLJ from 2 through 16 December 2002.

Figure 17 summarizes the crucial components of the meso- and synoptic scales of the case under study at 0600 UTC 7 February, when the spatial extent of the MCSs is greater than 200 000 km^2. In this figure, low-level circulation is denoted by streamlines at 1200 m, the location of the MCSs is indicated by the 218 K contour, the baroclinic area is represented by the contours of the meridional gradient of equivalent potential temperature $\nabla_m \theta_e$, and the SALLJ domain is represented by the area where the wind speed between the 2300- and 1700-m levels is greater than 6 m s^{-1} and the northerly wind component is greater than 12 m s^{-1}.

Figure 17 shows a strong northerly flow with a low-level jet profile to the north of 30°S. The SALLJ, which is active during the entire period under study, slows down over central Argentina, implying a large convergence zone at low levels in the area where MCSs developed. In addition, the figure clearly shows the deformation component of the kinematic field whose dilatation axis is in agreement with the frontal zone. The location of the MCSs in the figure represents the region where they spend most of their life cycles during the studied period. Such a structure allows us to assume that localized convergence and lifting motion at the front was important both in destabilizing the environment and in the initiation of convection.

As to instability in the region, differential thermal advection, along with moist advection within the layer from the surface to 4600 m, conditioned the environment to be favorable to the development of convection. Moisture advection continued favoring convection within the mentioned atmospheric layer; however, convective instability was quite localized and presented great spatial variability over central Argentina. On the other hand, the

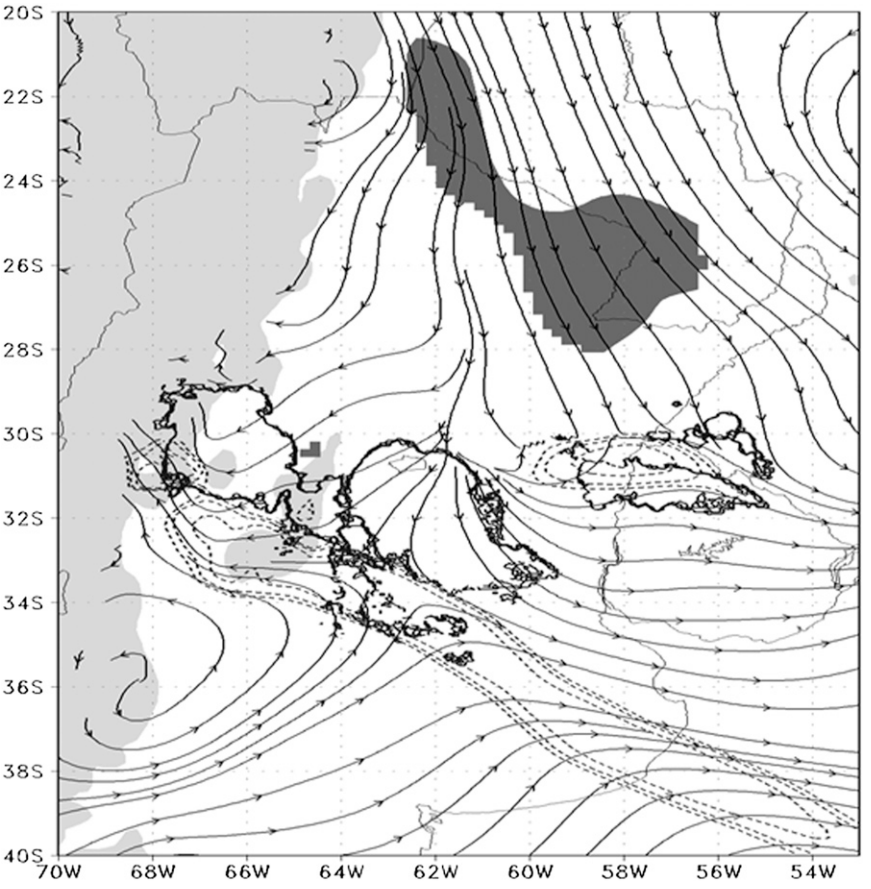

FIG. 17. Conceptual model of the different environmental patterns related to deep organized convection at 0600 UTC 7 Feb: orography higher than 800 m (light gray shading), 218-K brightness temperature (solid black contour), streamlines at 1200 m, regions with northerly wind speed stronger than 12 m s^{-1} at 1700 m and wind speed differences between 2900 and 1700 m greater than 6 m s^{-1} (dark gray shading), and meridional variation of θ_e greater than 7×10^{-5} K m^{-1} (dashed black contour).

region toward which the MCSs moved had more homogeneous values in terms of convective instability, allowing convective systems to develop in the entire region, in contrast with the genesis area where they developed over isolated regions.

Acknowledgments. This research was supported by Grants UBA X266, UBA X633, ANPCyT PICT 2006-1832 and ANPCyT PICT 07-14420. SALLJEX was funded by the PACS–SONET network and grants from FAPESP (01/13816-1) in Brazil; ANPCyT (PICT N°07-06671) and UBA (X055) in Argentina; and IAI–CRN (55), NSF (ATM0106776), NASA (NAG5-9717), and NOAA (PID-2207021 and NA03OAR4310096) in the United States. This research was carried out thanks to a scholarship from the University of Buenos Aires awarded to the first author. This paper was partially developed during the first author's stay at McGill University.

REFERENCES

Freitas, S. R., and Coauthors, 2009: The Coupled Aerosol and Tracer Transport model to the Brazilian developments on the Regional Atmospheric Modeling System (CATT-BRAMS)—Part 1: Model description and evaluation. *Atmos. Chem. Phys.,* **9,** 2843–2861.

García Skabar, Y., and M. Nicolini, 2009: Enriched analyses with assimilation of SALLJEX data. *J. Appl. Meteor. Climatol.,* **48,** 2425–2440.

Garreaud, R. D., 2000: Cold air incursions over subtropical South America: Mean structure and dynamics. *Mon. Wea. Rev.,* **128,** 2544–2559.

——, and J. M. Wallace, 1998: Summertime incursions of mid-latitude air into subtropical and tropical South America. *Mon. Wea. Rev.,* **126,** 2713–2733.

Janowiak, J. E., R. J. Joyce, and Y. Yarosh, 2001: A real-time global half-hourly pixel-resolution infrared dataset and its applications. *Bull. Amer. Meteor. Soc.,* **82,** 205–217.

Joyce, R. J., J. E. Janowiak, P. A. Arkin, and P. Xie, 2004: CMORPH: A method that produces global precipitation

estimates from passive microwave and infrared data at high spatial and temporal resolution. *J. Hydrometeor.,* **5,** 487–503.

Laing, A. G., and J. M. Fritsch, 2000: The large-scale environments of the global populations of mesoscale convective complexes. *Mon. Wea. Rev.,* **128,** 2756–2776.

Liebmann, B., G. N. Kiladis, J. A. Marengo, T. Ambrizzi, and J. D. Glick, 1999: Submonthly convective variability over South America and the South Atlantic convergence zone. *J. Climate,* **12,** 1877–1891.

Machado, L. A. T., W. B. Rossow, R. L. Guedes, and A. W. Walker, 1998: Life cycle variations of mesoscale convective systems over the Americas. *Mon. Wea. Rev.,* **126,** 1630–1654.

Maddox, R. A., 1983: Large-scale meteorological conditions associated with midlatitude, mesoscale convective complexes. *Mon. Wea. Rev.,* **111,** 1475–1493.

Marengo, J., W. Soares, A. C. Saulo, and M. Nicolini, 2004: Climatology of the low-level jet east of the Andes as derived from the NCEP–NCAR reanalyses: Characteristics and temporal variability. *J. Climate,* **17,** 2261–2280.

Nicolini, M., and A. C. Saulo, 2006: Modeled chaco low-level jets and related precipitation patterns during the 1997–1998 warm season. *Meteor. Atmos. Phys.,* **94,** 129–143.

——, ——, J. C. Torres, and P. Salio, 2002: Strong South America low-level jet events characterization during warm season and implications for enhanced precipitation. *Meteorologica,* **27,** 59–69.

Ruiz, J. J., 2010: Evaluation of different methodologies for CMORPH precipitation estimates calibration over South America. *Rev. Bras. Meteor.,* in press.

Salio, P., M. Nicolini, and C. Saulo, 2002: Chaco low-level jet characterization during the austral summer season. *J. Geophys. Res.,* **107,** 4816, doi:10.1029/2001JD001315.

——, ——, and E. J. Zipser, 2007: Mesoscale convective systems over southeastern South America and their relationship with the South American low- level jet. *Mon. Wea. Rev.,* **135,** 1290–1309.

Seluchi, M. E., C. Saulo, M. Nicolini, and P. Satyamuyty, 2003: The northwestern Argentinean low: A study of two typical events. *Mon. Wea. Rev.,* **131,** 2361–2378.

Velasco, I., and J. M. Fritsch, 1987: Mesoscale convective complexes in the Americas. *J. Geophys. Res.,* **92,** 9591–9613.

Vera, C., and Coauthors, 2006: The South American Low-Level Jet Experiment (SALLJEX). *Bull. Amer. Meteor. Soc.,* **87,** 63–77.

Vila, D. A., L. A. T. Machado, H. Laurent, and I. Velasco, 2008: Forecast and Tracking the Evolution of Cloud Clusters (ForTraCC) using satellite infrared imagery: Methodology and validation. *Wea. Forecasting,* **23,** 233–245.